Water Vapor Tomography Using GPS Phase Observations: Simulation Results

Tobias Nilsson and Lubomir Gradinarsky

Abstract—Global positioning system (GPS) tropospheric tomography normally requires that the slant wet delays between the GPS satellites and the ground receivers are estimated with high accuracy, which may be difficult given the presence of a number of error sources. This paper presents an alternative approach, namely to estimate the three-dimensional structure of the atmospheric water vapor directly from raw GPS phase observations. The method is tested in a number of simulations, where the impact of network size, the possible horizontal and vertical resolutions, the observation noise, and the inclusion of additional global navigation satellite systems were studied. The simulation results indicate that the refractivity field can be obtained with an accuracy of $\sim 20\%$ or better up to around 4 km with a height resolution of 1 km provided that a sufficient number of receivers and satellites is available.

Index Terms—Global positioning system (GPS), humidity, Kalman filtering, meteorology, simulation, terrestrial atmosphere, tomography.

I. INTRODUCTION

THE GLOBAL positioning system (GPS) is a useful tool for retrieving the total amount of integrated water vapor in the atmosphere [1]–[3]. Using a local network of GPS receivers, it is also possible to estimate the three-dimensional (3-D) structure of the wet refractivity of the atmosphere. This is done by using tomographic methods. These have been successfully applied to retrieve the electron content in the ionosphere [4]. For the troposphere, several different methods have been developed [5]–[11].

The application of GPS for tomographic retrieval of the water vapor distribution in the troposphere requires that the slant wet delays, i.e., the delay of the GPS signals in the atmosphere due to water vapor between each satellite and each receiver, are estimated from the GPS phase data recorded by the receivers. To retrieve the 3-D structure of the wet refractivity, the troposphere is divided into a finite number of boxes (normally called voxels, finite volume pixels) where the refractivity is assumed to be constant. By doing this discretization, the slant wet delays can be described as linear combinations of the refractivities of the voxels; hence the refractivity field can be obtained by solving a linear system of equations.

To retrieve the slant wet delays from the GPS data, the delays are modeled as functions of a number of unknown parameters. Normally, a slant wet delay is modeled as being a function of a zenith wet delay and a gradient [5]. This model is then used in GPS data processing, where the model parameters are estimated along with other unknowns contributing to the signal delays. The residuals of the processing are then considered to contain the unmodeled part of the slant wet delays. Hence, slant wet delays can be obtained by adding the residuals to the slant wet delays calculated from the retrieved zenith wet delays and gradients.

However, it is not obvious that the retrieved slant wet delays will be accurate enough. The parts of the delays due to water vapor not modeled by the zenith delays and the gradients might be absorbed in the estimation of other unknown parameters in the GPS processing, like clock errors. Even for ideal conditions, the slant wet delays retrieved in this way may not be very accurate [12]. Hence, some of the information about the 3-D structure of the wet refractivity contained in the slant wet delays may be lost in this process. Consequently, the refractivity field retrieved using these slant wet delays in GPS tomography may contain unacceptable errors.

In this paper, a new method to retrieve the 3-D structure of the water vapor is presented. Instead of using one model for the slant wet delays in GPS processing and then applying another model to retrieve the wet refractivity field, we apply the voxel discretization of the wet refractivity field already in the GPS processing step. Hence, slant wet delays are described as linear combinations of the refractivities of voxels in GPS processing. This has the advantage that any error arising from the modeling of slant wet delays in terms of zenith delays and gradients will disappear. Another advantage is that the number of steps required to obtain the wet refractivity field is reduced.

The disadvantage is of course that there are many parameters that need to be estimated in the processing. It can be shown that apart from the refractivity of the voxels, the parameters needed to be estimated will be errors in the satellite and the receiver clocks. However, the clock errors need to be estimated (alternatively removed using differencing methods) anyway, and there are no reasons why the effect of clock error estimation should be less if it is done in the first step before the tomographic estimation of refractivities. Also, the number of additional parameters needed to be estimated will be small compared to the number of observations if there are many satellites and receivers available. Given N satellites and M receivers, there will be $N * M$ observations at each epoch and $N + M$ clock errors to be estimated, and if N and M are large,

then $N * M \gg N + M$; hence the cost of estimating the additional clock errors will be low.

The new method was briefly described in [13], where a few simulation results were also presented. In Section II, we present the method in greater detail. The theory of this method requires retrieving the integer ambiguities of the observed GPS phases. In Section III, we demonstrate the accuracy of this retrieval. In Section IV, to assess its capabilities, we test the method through simulations. In the simulations, we also test the impact of including data from other global navigation satellite systems (GNSSs) and the possibility to use the method in real time. Our conclusions are presented in Section V. A comparison is also made with more simple methods, like estimating the refractivity using only one GPS receiver. These are presented in Appendix III.

II. THEORY

The observed carrier phase (expressed in units of length) L_i^j of the GPS signal from satellite j observed by receiver i can be written as [14]

$$L_i^j = \rho_i^j + \tau_i + \tau^j + I_i^j + l_i^j + M_i^j \lambda + \epsilon_i^j \qquad (1)$$

where

ρ_i^j distance between the satellite and the receiver;
τ_i and τ^j errors in the receiver and the satellite clocks;
I_i^j and l_i^j ionospheric and tropospheric delays between the satellite and the receiver;
M_i^j integer ambiguity;
λ wavelength of the signal;
ϵ_i^j phase measurement error. This term will contain the not modeled contributions to the observed phase, e.g., receiver noise, multipath, etc.

The distance between the satellite and the receiver can be calculated if we know their positions. In a permanent ground network, the receiver positions could be known with an accuracy of a few millimeters. Satellite positions, however, generally have an accuracy of $\sim$5 cm [15]. For a dense network of receivers, a small error in satellite position will introduce approximately the same errors in the distances to the satellite for all receivers, i.e., $\delta\rho_i^j \approx \delta\rho^j$. For example, the difference in error in the observed phases of two stations separated by 10 km caused by a 20-cm satellite position error will be around 0.1 mm. Hence, an error in the satellite position will have approximately the same effect as an error in the satellite clock.

The tropospheric delay is

$$l_i^j = 10^{-6} \int N dl$$

$$= 10^{-6} \int N_h \, dl + 10^{-6} \int N_w \, dl$$

$$= (l_h)_i^j + (l_w)_i^j \qquad (2)$$

where the indices h and w denote the hydrostatic and wet parts, and N is the refractivity ($N = 10^6(n - 1)$, n being the refractive index). The hydrostatic part of the delay in the zenith direction can be approximated if the ground level pressure is measured at the receiver location (see Appendix I). The hydrostatic delay in the slant direction can then be calculated from the hydrostatic zenith delay using a mapping function [16].

Letting $\hat{L}_i^j = L_i^j - (\rho_0)_i^j - (l_h)_i^j$, where $(\rho_0)_i^j$ is the approximate distance from the available satellite positions, we rewrite (1) as

$$\hat{L}_i^j = \tau_i + \tau^j + \delta\rho^j + I_i^j + (l_w)_i^j + M_i^j \lambda + \epsilon_i^j. \qquad (3)$$

For phase observations, the integer ambiguities and clock errors are partly indistinguishable. For example, an increase in all ambiguities of one satellite will have the same effect on the phase observations as an increase in that satellite's clock. This makes it possible to consider parts of the ambiguities as clock errors, hence reducing the number of ambiguities needed to be estimated. More precisely, we can include all ambiguities of one satellite (for example, satellite number 1) and all ambiguities of one receiver (receiver number 1) as additional contributions to the satellite and receiver clock errors. The remaining parts of the integer ambiguities, which need to be estimated, will then be $\hat{M}_i^j = M_i^j - M_1^j - M_i^1 + M_1^1$. Now (3) can be written as

$$\hat{L}_i^j = \tau_i + M_i^1 \lambda + \tau^j + \delta\rho^j + M_1^j \lambda$$
$$- M_1^1 \lambda + I_i^j + (l_w)_i^j + \hat{M}_i^j \lambda + \epsilon_i^j$$
$$= \hat{\tau}_i + \hat{\tau}^j + I_i^j + (l_w)_i^j + \hat{M}_i^j \lambda + \epsilon_i^j \qquad (4)$$

where $\hat{\tau}_i = \tau_i + M_i^1 \lambda$ and $\hat{\tau}^j = \tau^j + \delta\rho^j + M_1^j \lambda - M_1^1 \lambda$. The new integer ambiguities $\hat{M}_i^j$ can be estimated by taking the double difference [14] of (4) as (note that $\hat{M}_1^j = \hat{M}_i^1 = 0$)

$$\hat{L}_{i1}^{j1} = \hat{L}_i^j - \hat{L}_i^1 - \hat{L}_1^j + \hat{L}_1^1$$
$$= I_{i1}^{j1} + (l_w)_{i1}^{j1} + \left(\hat{M}_i^j - \hat{M}_i^1 - \hat{M}_1^j + \hat{M}_1^1 \right) \lambda + \epsilon_{i1}^{j1}$$
$$= I_{i1}^{j1} + (l_w)_{i1}^{j1} + \hat{M}_i^j \lambda + \epsilon_{i1}^{j1}. \qquad (5)$$

For a dense network of receivers, I_{i1}^{j1}, $(l_w)_{i1}^{j1}$, and ϵ_{i1}^{j1} will all be small compared to λ (at least for signals observed at high elevation angles), so $\hat{M}_i^j$ can be estimated by

$$\hat{M}_i^j = \text{INT} \left[\frac{\hat{L}_{i1}^{j1}}{\lambda} \right] \qquad (6)$$

where INT denotes rounding off to the nearest integer. An integer ambiguity will not change as long as the receiver tracks the satellite. Hence, if no cycle slips occur, an ambiguity only needs to be estimated once for each period the satellite is visible.

The ionospheric delay can be eliminated by using two frequencies and forming the ionospheric free combination [14].

Defining

$$\bar{L}_i^j = \hat{L}_i^j(f) - \lambda \hat{M}_i^j(f) \tag{7}$$

$$\tilde{L}_i^j = \frac{f_1^2 \bar{L}_i^j(f_1) - f_2^2 \bar{L}_i^j(f_2)}{f_1^2 - f_2^2} \tag{8}$$

$$\tilde{\tau}_i = \frac{1}{f_1^2 - f_2^2} \left(f_1^2 \hat{\tau}_i(f_1) - f_2^2 \hat{\tau}_i(f_2) \right) \tag{9}$$

$$\tilde{\tau}^j = \frac{1}{f_1^2 - f_2^2} \left(f_1^2 \hat{\tau}^j(f_1) - f_2^2 \hat{\tau}^j(f_2) \right) \tag{10}$$

$$\tilde{\epsilon}_i^j = \frac{1}{f_1^2 - f_2^2} \left(f_1^2 \epsilon_i^j(f_1) - f_2^2 \epsilon_i^j(f_2) \right) \tag{11}$$

we obtain

$$\tilde{L}_i^j = \tilde{\tau}_i + \tilde{\tau}^j + (l_w)_i^j + \tilde{\epsilon}_i^j. \tag{12}$$

The ordinary ionospheric free combination used in (8) removes the first-order ionospheric effect. However, during periods of high ionospheric activity, we may also need to consider higher order ionospheric effects. Methods for also removing some of the higher order effects exist [17]. In [18], it is shown that with the future modernization of GPS (including a third frequency), the ionospheric effect of the second and third orders may also be removed. However, in this paper, we assume that the effect of the ionosphere is completely removed by using (8).

If we make a discretization by assuming that the wet refractivity field can be described by a linear combination of a number of base functions, the wet tropospheric delay can be described as a linear combination of these base functions integrated along the signal path. A common and simple choice of base functions is voxels, meaning that the 3-D space is divided into a number of boxes (voxels). In every voxel, the wet refractivity N_w is assumed to be constant. Using this discretization, the wet tropospheric delay can be expressed as

$$(l_w)_i^j = 10^{-6} \int N_w \, dl = 10^{-6} \sum_{k=1}^{n} N_w(k) x_i^j(k) \tag{13}$$

where n is the number of voxels and $x_i^j(k)$ is the length of the ray from satellite j to receiver i in voxel k. If s_m denotes the satellite transmitting ray number m and r_m denotes the receiver receiving ray m, (12) can now be written as

$$\tilde{L}(m) = \tilde{L}_{r_m}^{s_m} = \tau_{r_m} + \tau^{s_m} + 10^{-6} \sum_{k=1}^{n} N_w(k) x_{r_m}^{s_m}(k) + \tilde{\epsilon}(m)$$

$$= \tau_r(m) + \tau^s(m) + 10^{-6} \sum_{k=1}^{n} N_w(k) x(m,k) + \tilde{\epsilon}(m) \tag{14}$$

where $x(m,k)$ is the length of ray m in voxel k. By writing this equation for all rays, we form a linear system of the form $\mathbf{y} = \mathbf{Ax}$, where the unknowns ($\mathbf{x}$) are the voxel refractivities and the satellite and the receiver clock errors.

The system will however in general be ill conditioned due to poor voxel coverage in some areas caused by limited ray geometry [10]. If we would use a flat grid, i.e., model the troposphere as a number of flat layers with all stations in the lowest layer, it would be impossible to retrieve the refractivity field if the number of layers were larger than two (with all stations located in the lowest layer). This can easily be realized by noting that in such a case an increase of the refractivity in one layer could be compensated by a decrease in another layer, leaving the slant wet delays unchanged. To avoid this problem, we do not use a flat grid but a grid following the curvature of the Earth. However, since this curvature is small, we will still have a very weak geometry. To solve the system, additional information must be included. One approach would be to add a set of smoothing equations $\mathbf{Bx} = \mathbf{0}$ as in, e.g., LOcal Tropospheric TOmographic Software (LOTTOS) [5], or to implement a Kalman filter [19] as in Wet Refractivity Kalman Filter (WeRKaF) [10], [11]. Here, the Kalman filter approach has been chosen (see Appendix II).

III. TEST OF AMBIGUITY DETERMINATION

The proposed method requires that the integer ambiguities are correctly estimated. This is possible if $I_{i1}^{j\bar{1}}$ and $(l_w)_{i1}^{j1}$ in (5) (as well as the observation noise) are small compared to λ. Otherwise, the ambiguities determined by (6) can be in error. To test how well the ambiguities can be determined, an investigation using real data from the local GPS network in Göteborg, Sweden, was performed. We calculated $\Delta_i^j = \hat{L}_{i1}^{j1}/\lambda - \hat{M}_i^j$ [where $\hat{M}_i^j$ is determined by (6)] for all observations above a minimum elevation (set to $5°$ in this investigation). If the majority of the observations are $\Delta_i^j \approx 0$, and very few (or none) observations are $\Delta_i^j \approx \pm 1/2$, then the ambiguities have probably been determined correctly.

In Fig. 1, the distributions of Δ_i^j for the two GPS frequencies L1 ($\lambda = 19.0$ cm) and L2 ($\lambda = 24.4$ cm) are displayed. Here, the interval $[-1/2, 1/2]$ is divided into 200 subintervals. We then plot the number of observations in each subinterval. Data from two of the stations separated by ~ 8.4 km were used. The data were collected on July 4, 2001, between 00:00 coordinated universal time (UTC) and 15:00 UTC using a 15-s sampling interval.

As seen in the figure, most of the values are close to zero, and very few are close to $\pm 1/2$ (less than 0.04% of all observations with $|\Delta_i^j| > 0.95 \cdot 1/2$). Those with high values have a low elevation angle. If there are no cycle slips, the ambiguities will not change, so it is sufficient to estimate the ambiguities at high elevations and then check that no cycle slips occur at lower elevations. All other investigated days gave similar results. Hence, we can conclude that the ambiguities can be correctly estimated. It should be noted that the amount of data available was limited (May–August in 2001 and 2002); thus, it cannot be excluded that under very extreme conditions the ambiguity resolution technique used here could fail.

The accuracy of the ambiguity estimations deteriorates for longer baselines (> 50 km), which we will normally not have in a typical GPS tomographic network. Also, over such large distances, the contribution to Δ_i^j from the wet part of the tropospheric delay may not be negligible. In case such longer baselines are used, a way to improve the situation may be to first estimate the ionospheric delays to remove most of the errors associated with the ionosphere.
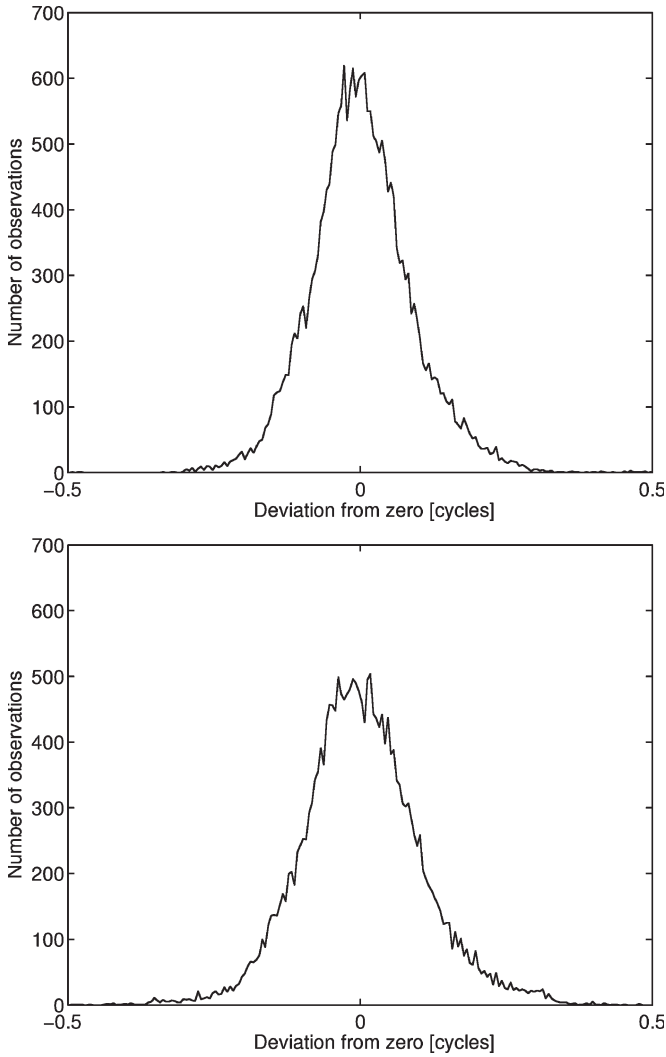
Fig. 1.   Distribution of $\Delta_i^j = \hat{L}_{i1}^{j1}/\lambda - \hat{M}_i^j$ for (top) L1 and (bottom) L2.
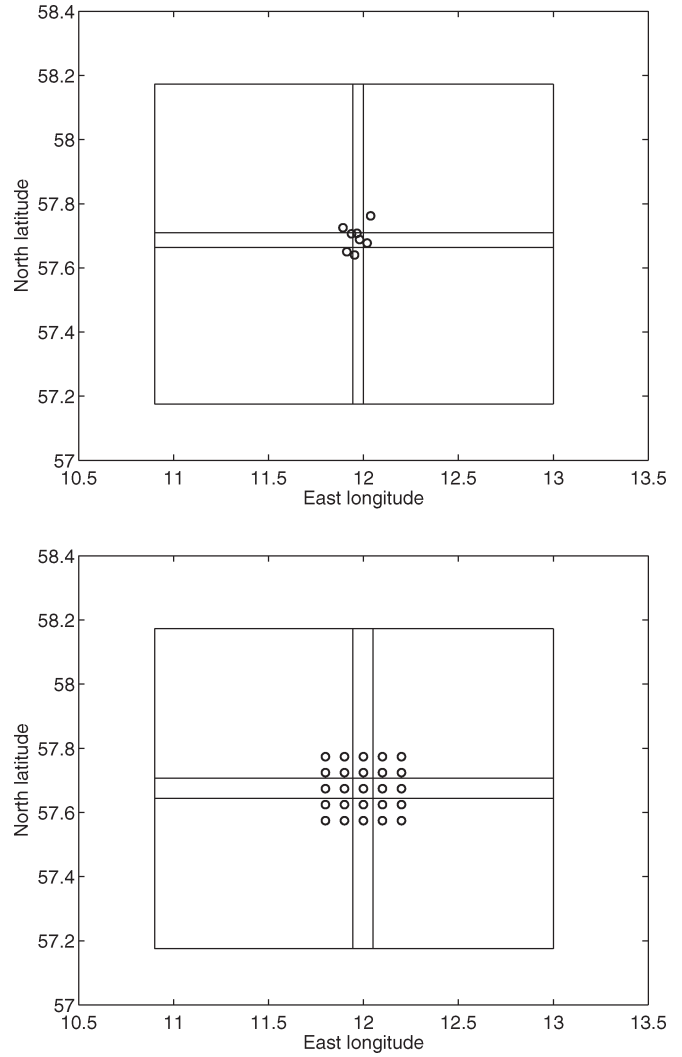

Fig. 2.   The 3×3 grid together with (top) the eight-station network and (bottom) the 25-station network.

IV. SIMULATION RESULTS

A. Simulation Setup

We used two different networks, namely: 1) the existing network in Göteborg consisting of eight sites and 2) a (nonexisting) network of 25 sites. The sites of the latter were uniformly distributed in longitude and latitude, and their heights were uniformly randomly distributed between 0 and 100 m. The heights of the stations in the eight-station network varied from 55 to 170 m above the ellipsoid. In Fig. 2, the two different networks are displayed together with the 3×3 grid used in most of the simulations. The outer voxels were chosen to be larger than the voxels in the middle (where the stations are located) to allow for many rays to cross horizontal voxel borders and at the same time allow for observations at low elevation angles. However, it should be noted that in cases where the atmosphere is very variable horizontally, problems arising from the assumption of constant refractivity might occur. In height, we used a voxel size of 1000 m and eight layers (hence assuming that there is no significant amount of water vapor present above 8000 m, which is a reasonable assumption for these latitudes).

The geometry of the voxel grid is good if there are many observations that cross many voxels. For the eight-station network, the average number of observations for each epoch is 57.4. Using the grid in Fig. 2 (top), the average number of observations crossing 8, 9, 10, 11, and 12 voxels are 11.6, 17.2, 19.6, 7.3, and 1.7, respectively. There were no observations crossing more than 12 voxels and no less than eight since at least eight voxels will be crossed if the rays are to exit the grid at the top. If we, instead, would have used a grid with voxels all having the same horizontal sizes (keeping the size of the area covered the same), on average 43.0 crossed only eight voxels, and on average there were 11.5 and 2.8 observations crossing nine and ten voxels, respectively. No rays crossed more than ten voxels. This indicates that using a more uniform grid discretization, the equation system (14) would be weaker.

We first simulated the refractivity field from which we then calculated the slant wet delays between the stations and the satellites. To these we added the simulated integer ambiguities, the clock errors, the hydrostatic delay errors, the ionospheric delays, and the observation noise. Errors were also added to the satellite positions (in all three coordinates). Then, we applied

our method to estimate the ambiguities and used these to correct the observations. After that, the ionospheric delays were removed, and the resulting observations were put into the Kalman filter to estimate the voxel refractivities (and the clock errors). The Kalman filter loop was run both forward and backward.

In most simulations, the clock errors were described as white noise processes with a standard deviation of 1.7 ms $(5 \times 10^5$ m), which are of the same order or worse than that of real clock errors. However, the magnitude of the clock errors will not have a large impact on the results since they need to be estimated. The errors in the satellite position had a standard deviation of 0.2 m, which is somewhat more uncertain than the International GNSS Service (IGS) final orbits (rms error of 5 cm) but close to the IGS rapid orbits [15]. The errors in the hydrostatic delays were assumed to originate from uncertainties in pressure measurements having a standard deviation of 0.2 mbar. The wet refractivity profiles were based upon real profiles obtained from radiosonde launches at the Landvetter airport outside Göteborg, and a gradient of 0.14 mm/km in the northeast direction was used in most simulations (a reasonable value for the Göteborg area [20]). We used a sampling interval of 120 s (which turned out to be sufficient). The measurement noise was assumed to be white, a reasonable assumption when the sampling period is larger than 10 s [21].

B. Refractivity Estimation for Two Networks

As a first case, we tested the retrieval of wet refractivity profiles constant in time. We performed two simulations for each of the networks in Fig. 2, one with an exponential profile and one with a profile with a strong inversion. An rms observation noise of 5 mm was used. The simulated period was 14.5 h (of this period, the last 12 h were used to check the solution, giving the Kalman filter 2.5 h to converge). The retrieved profiles 5 h after the start of the simulated period are shown in Fig. 3. Shown are the profiles of the central voxel column. The error bars are the formal error from the estimation covariance matrix in the Kalman filter [19]. The retrieved profiles at later times were approximately the same.

For the exponential profile, both networks retrieved the shape rather well, and as expected, the 25-station network resulted in a better agreement. Calculating the absolute mean estimation error for all voxels and all time epochs in the last 12 h of the simulations gave an average error of 2.05 mm/km for eight stations and 1.10 mm/km for 25 stations. The absolute error is largest in the lower atmosphere. For the eight-station network, the mean estimation error for the first 4 km of the troposphere was 3.38 mm/km, while only 0.71 mm/km for the top 4 km. The corresponding values for the 25-station network were 1.67 and 0.53 mm/km.

For the profile with an inversion, the eight-station network does not detect the inversion quickly. However, it detects it after a longer time (> 12 h). At the end of the simulation period, it can be seen that an inversion has been detected, although not matching its magnitude. The 25-station network, on the other hand, clearly detects the inversion. The mean estimation error is 7.72 mm/km for the eight-station network and 2.79 mm/km for the 25-station network. However, the mean error of the eight-
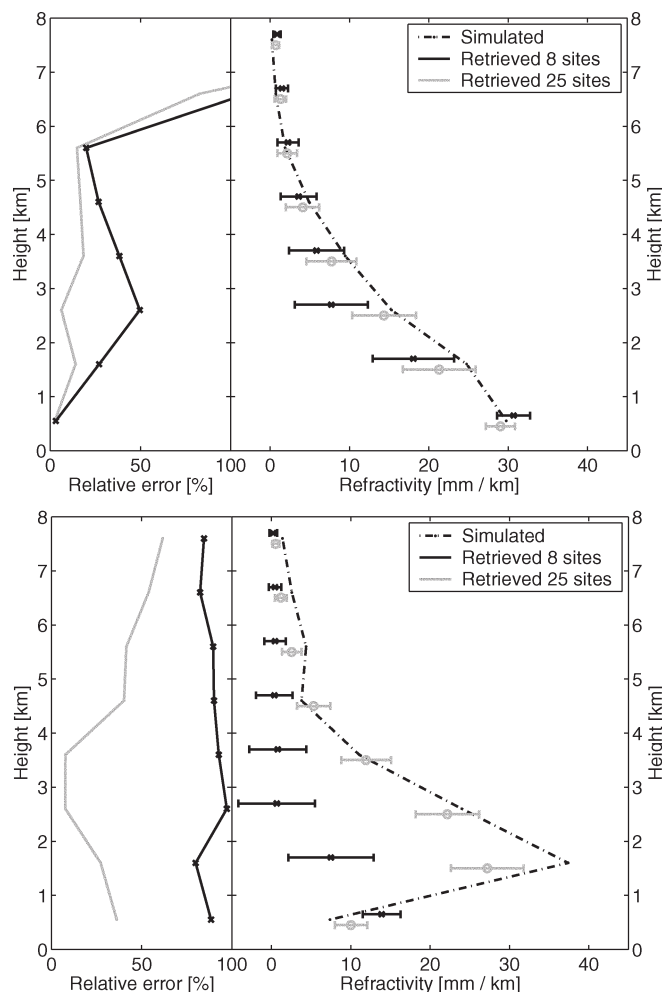

Fig. 3. Simulated and estimated refractivity profiles after 5 h. The rms observation noise was 5 mm. In this and the other figures, the retrieved solutions are offset in height from the center of the voxel height for better visibility.

station network solution is decreasing with time and is around 4.4 mm/km at the end of the simulation. The mean estimation error for the first 4 km was 13.27 mm/km using eight stations and 4.02 mm/km using 25 stations.

Fig. 3 also displays the relative error, i.e., the relative deviation between the simulated and retrieved refractivities. For the exponential profile, the relative error is larger than 100% for the top layers. This indicates that the method is not suitable for retrieval of the wet refractivity high up in the troposphere, where the amount of water vapor is low.

A more realistic case is a wet refractivity profile that changes with time. Initially, the profile was almost exponential. At time 6:00, the refractivity around a height of 2 km began to increase. The increase continued until 12:00. After that, the refractivity started to decay back to its original shape, a state reached at 18:00. The rms observation noise was chosen to be 10 mm. In Fig. 4, the simulated and estimated profiles at 9:00 and 13:00 are shown. As seen, the 25-station network retrieves the profile better than the eight-station network at the lowest layer. However, the 25-station network is slightly worse at a height of between 3 and 5 km at 13:00. This is probably a consequence of the correlations between the voxel refractivities used in the Kalman filter, which do not completely allow for the rather
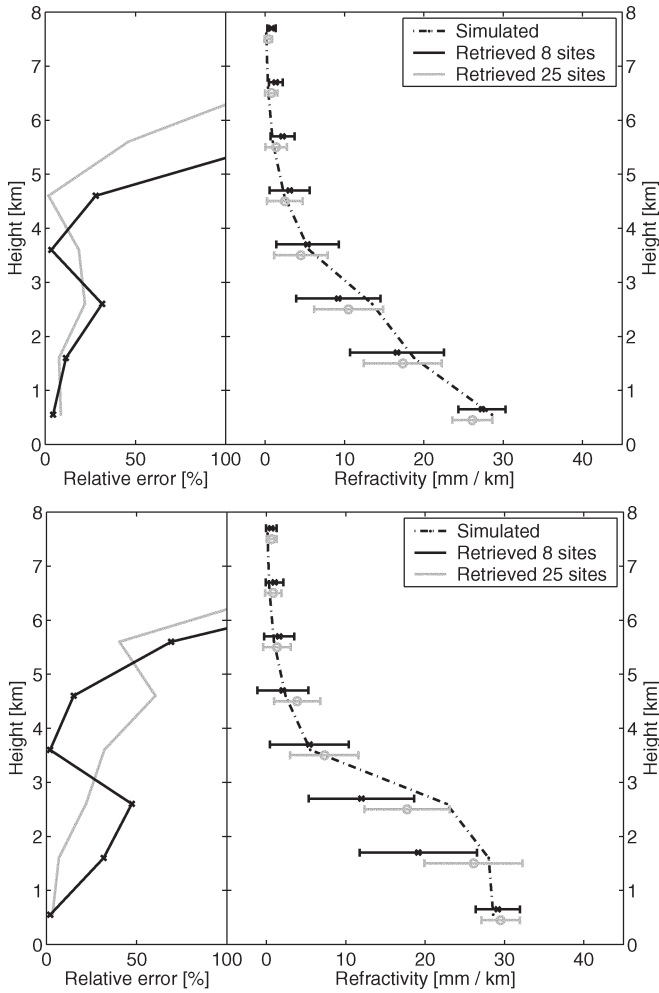
Fig. 4. Simulated and estimated wet refractivity profiles using eight and 25 stations at (top) 9:00 and (bottom) 13:00. An increase in the refractivity occurred around a height of 2 km between 6:00 and 12:00; then the profile decayed back to normal until 18:00. The rms observation noise was 10 mm.

large decrease in the refractivity between the third and fourth layers. As a consequence, the refractivity above 3 km is slightly overestimated. The average estimation errors between 6:00 and 18:00 were 1.85 and 1.28 mm/km for the eight-site and 25-site networks, respectively. As before, the errors were larger for the lower heights; the average estimation errors for the first 4 km were 2.97 and 2.18 mm/km using eight and 25 stations, respectively.

C. Observation Noise Sensitivity

We investigated the sensitivity of the methods to observation noise in the receivers using the 25-station network. We used a constant profile having an inversion at ∼1.5 km. The rms noise was varied from 0 to 15 mm.

In Fig. 5, the average estimation error is plotted as a function of the rms observation noise. It should be noted that this noise does not represent all the noise present in the GPS signals. Additional noise components could arise from errors in the estimation of hydrostatic delay and from errors in satellite positions. The results demonstrate that for an rms noise of less than 10 mm, the retrieved profile will not be affected significantly.
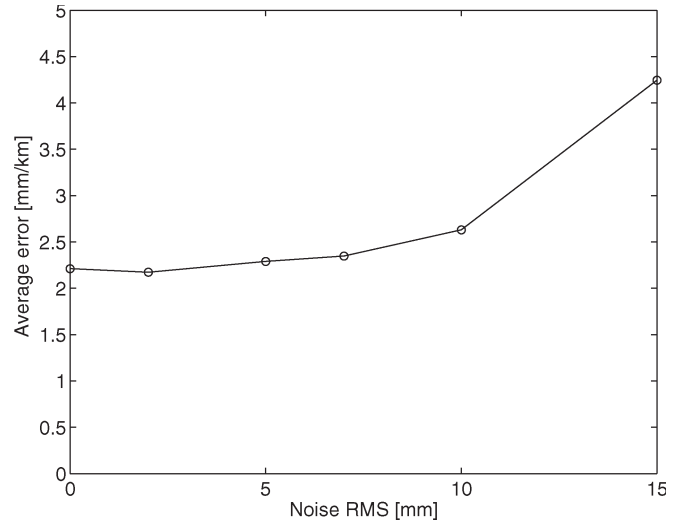

Fig. 5. Test of the sensitivity to noise. Plotted are the mean estimation errors of the retrieved refractivity as a function of rms observation noise using the 25-station network and a constant profile having an inversion at ∼1.5 km.

D. Inclusion of Other GNSS

One possible way to improve the estimation of refractivity is to increase the number of observations by including data from other GNSSs such as the Russian system GLONASS [22] or the future European system Galileo [23]. Note that since these systems use other frequencies than GPS, we will have to include additional receiver clock error terms for each system.

A simulation was performed using both GPS and Galileo. The refractivity profile used was the same as in Fig. 4, and the rms observation noise was 10 mm. The result using the eight-station network is presented in Fig. 6 (the GPS-only case is also plotted for comparison). The mean estimation error decreased from 1.85 to 1.78 mm/km when using both systems. We can observe a similar decrease in accuracy above 3 km as we did in the case of the 25-station network; the explanation for this is the same as before. It can be seen that the error for the top 4 km is larger when using GNSS, on average 1.08 mm/km, while the GPS-only case being only 0.74 mm/km. For the first 4 km, the mean estimation error decreased to 2.48 mm/km (from 2.97 mm/km). We did not observe any improvement for the 25-station network when also including Galileo (mean estimation error of 1.3 mm/km).

E. Grid Resolution Test

With the 25-station network, it might be possible to get a better resolution using more voxels, either horizontally or vertically (or both). To test the possibility of using higher horizontal resolution, simulations based on a 5 × 5 grid were made. The grid was chosen such that each horizontal voxel would contain one station. In Fig. 7, the grid is displayed together with the locations of the stations.

In Fig. 8, the results of simulations using the changing profile in Fig. 4 are shown. Two simulations were made, one with GPS only and one with both GPS and Galileo. When using GPS only the errors were (as could be expected due to more unknown quantities) somewhat larger than for the 3 × 3 network,
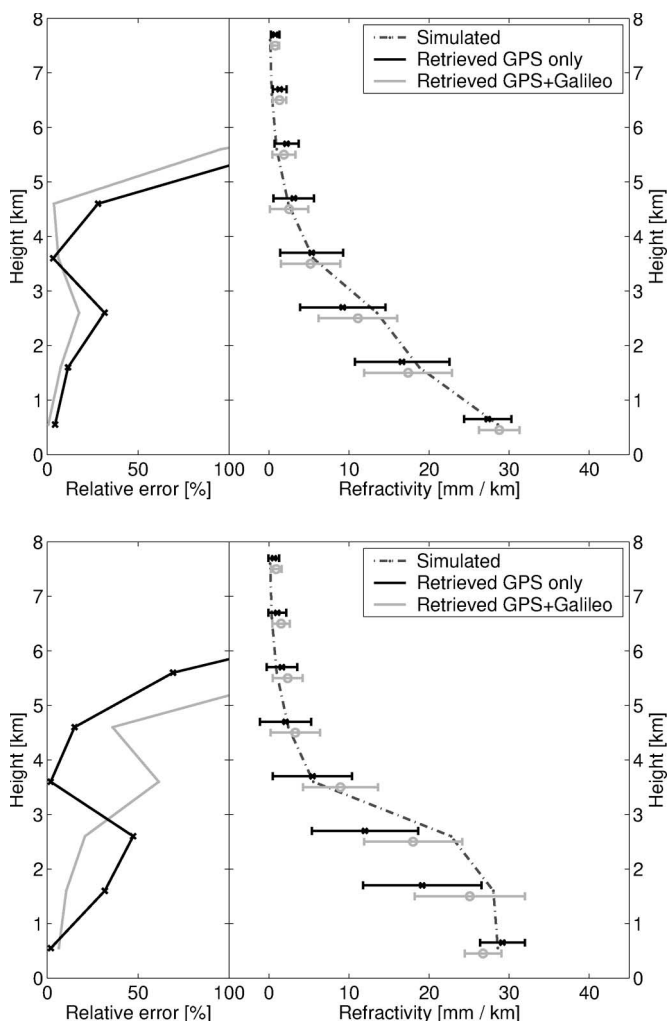
Fig. 6. Simulated and estimated wet refractivity profiles using GPS only and GPS + Galileo at (top) 9:00 and (bottom) 13:00 for the eight-station network. The rms observation noise was 10 mm.
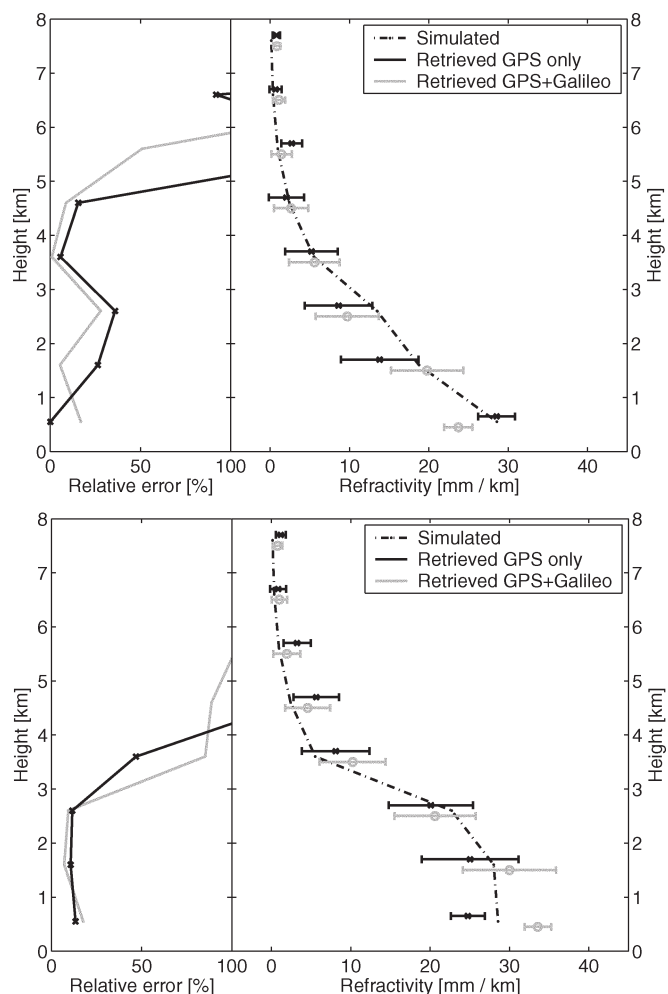

Fig. 8. Simulated and estimated wet refractivity profiles for the 5 × 5 grid at (top) 9:00 and (bottom) 13:00. The rms observation noise was 10 mm.
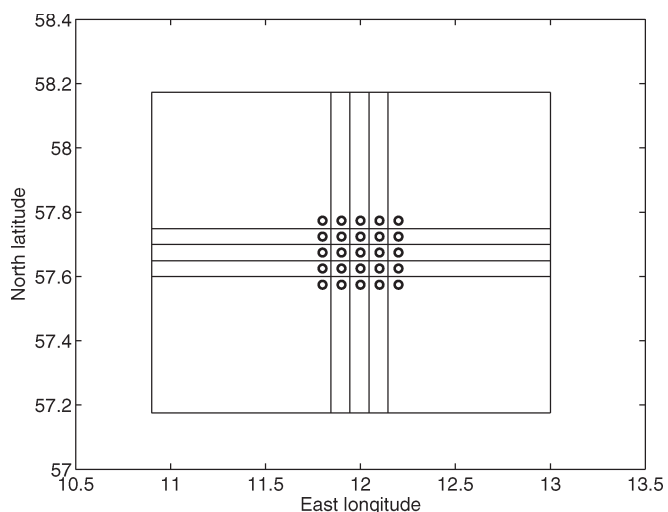

Fig. 7. The 5 × 5 grid together with the 25-station network.

with mean estimation error of 2.01 mm/km. When using both GPS and Galileo a mean estimation error of 1.78 mm/km was obtained.

A test of the height resolution was performed using the 25-station network. The 3 × 3 grid was used, but now with 16 layers (height resolution of 500 m). A constant refractivity profile with an inversion and some structures of size ~500 m were used. Two simulations were made: one with rms observation noise of 5 mm and one with rms observation noise of 10 mm. The result, as seen in Fig. 9, shows that the inversion around 1250 m was not completely detected, but otherwise the refractivity was retrieved well. The mean estimation error was 2.23 mm/km with rms observational noise of 5 mm, and 2.94 mm/km for 10 mm.

One way to improve the geometry of the problem might be to use a more advanced grid, where the heights of the voxels in a horizontal layer are not equal. In this way, the problem with the system being ill conditioned due to a nearly flat grid might be avoided. We have made simulations where more advanced grids have been tested, e.g., a grid where we use eight layers in height in the middle of the grid and seven layers elsewhere. The results were inconclusive: the increase in refractivity occurring around midday in the profile of Fig. 4 was detected much better with the eight-station network and using GPS only when using a more advanced grid, but instead the profile at the end of the simulation (18:00) was not retrieved as accurately.
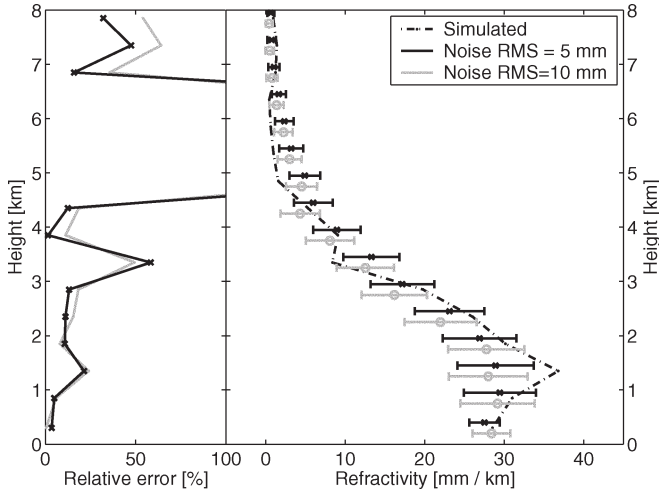
Fig. 9.   Result of a height sensitivity test using a profile constant in time. The results of two simulations are shown; the rms observational noise were 5 mm in one simulation and 10 mm in the other.

F. Network Considerations

The ability to retrieve the refractivity using a network of GPS receivers will not only depend on the number of receivers in the network but also be dependent upon the geometry of the network. For example, a network where the stations have larger spreads in the vertical direction will retrieve the refractivity better than a network where the stations are at the same height. In the case where there are two stations located in the same voxel but at different heights, the local geometry in the voxel will be strong, creating a better condition to obtain the refractivity of the voxel correctly. In the simulations performed above, networks with some ($\sim$100 m) differences in height have been used, but larger height differences may improve the results. To demonstrate the above, two simulations were carried out: one using a network where the stations were at exactly the same height and one with a spread in height. Both networks consisted of nine stations. In the latter, the height spread was 1200 m. The refractivity was the same as used in Fig. 4, and the rms observation noise was 10 mm. The result can be seen in Fig. 10. The mean estimation error was 2.83 mm/km for the former and 1.56 mm/km for the latter, where there were stations located in both the first and second layers, causing the refractivity in both the first and second layers to be retrieved with high accuracy.

G. Gradient Estimations

So far, we have only investigated the estimation of vertical profiles. However, using our method, one could also retrieve horizontal variations of wet refractivity. One way to assess the estimation of horizontal variations is to look at zenith delay gradients. The zenith delay gradient is defined as [24]

$$\vec{G} = 10^{-6} \left[\nabla_{\vec{\rho}} \int_{0}^{\infty} N_w(\vec{\rho}, z) dz \right]_{\vec{\rho}=0} \quad (15)$$

where $\vec{\rho}$ is the horizontal position vector and z is the height. If the integrated refractivity is assumed to change linearly, the
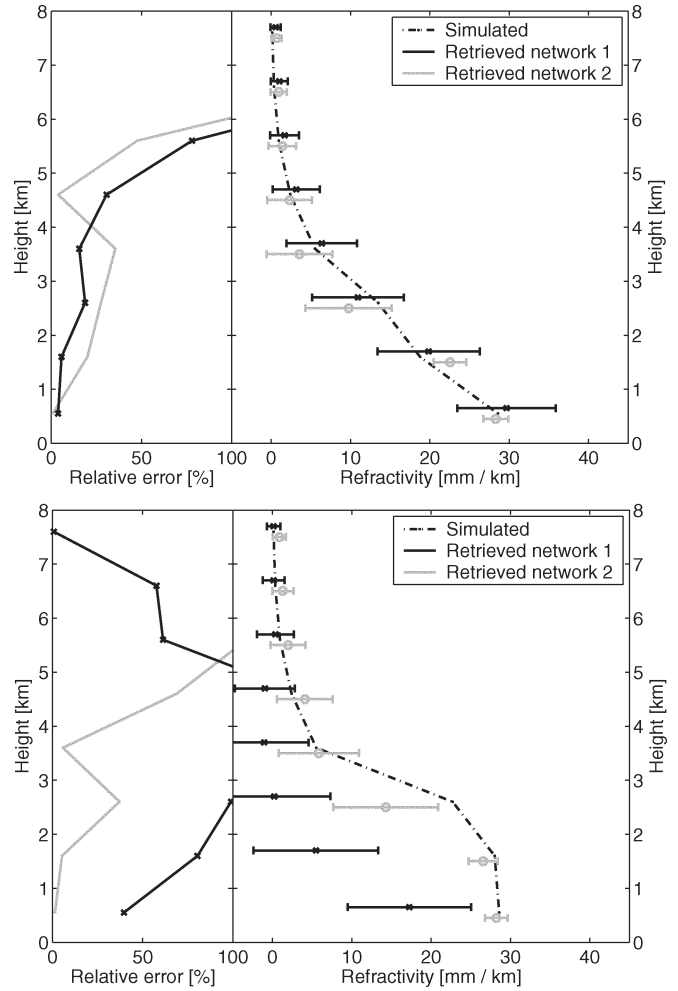

Fig. 10.   Simulated and estimated wet refractivity profiles for two nine-station networks: one with the stations at the same heights (network 1) and one with stations at different heights (network 2). Shown are the profiles at (top) 9:00 and (bottom) 13:00. The rms observation noise was 10 mm.

gradient can be estimated if the integrated refractivities are known above at least three sites.

A few simulations were made using the eight- and 25-station networks, and assuming different gradients. By integrating the retrieved refractivities from the ground to the top of the troposphere at the horizontal midpoints of each voxel, the gradient was estimated using a least square fit to (15). Here, an assumption that the retrieved refractivity will be equal to the refractivity in the middle of the voxel was made. In general, this will not be true: the refractivity of a voxel will be some average of the refractivity where the rays are crossing the voxel. Since the stations are all located close to the middle of the grid, most rays will be close to the middle of the grid, especially at the lower layers. Hence, the estimated refractivity of an outer voxel may not be equal to the refractivity in the middle of the voxel, but rather the refractivity at a point in the voxel closer to the middle of the grid. As a consequence, the estimated gradients will be underestimated.

In Fig. 11, the retrieved gradients are plotted as a function of time. The result was obtained using the 25-station network and the 5 × 5 grid in Fig. 7 for higher horizontal resolution. The gradient used in the simulation was 0.1 mm/km in the north
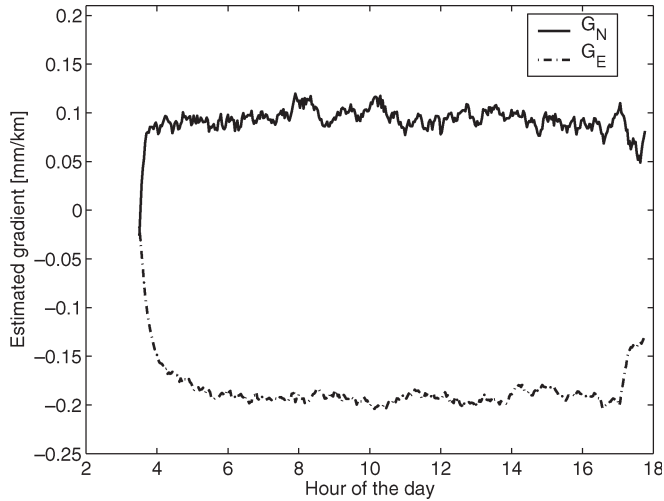
Fig. 11. Retrieved north (solid line) and east (dotted–dashed line) gradients. The mean north and east gradients are 0.094 and −0.189 mm/km, respectively (the simulated values were 0.1 and −0.2 mm/km).

direction and −0.2 mm/km in the east direction. As expected, the retrieved gradients were slightly lower than the simulated ones, about 95% (the retrieved gradients were on average 0.094 mm/km in the north direction and −0.189 mm/km in the east direction). In general, the standard deviations of the gradient estimations were about 0.01 mm/km. The reason for the gradient not being estimated very well in the beginning of the simulation is because the estimated refractivity in the beginning will be highly dependent on the initial guess (which assumed no gradient).

H. Inclusion of Ground Data

A possible way to improve the tomographic retrieval might be to include measurements of the wet refractivity at ground level. Of course, the ground level wet refractivity is not equivalent to the refractivity of a voxel. However, assuming that several measurements of the wet refractivity on different places in the voxels of the lowest layer could be available, the refractivity of these voxels could be estimated rather well. In Appendix III, it is shown that using one measurement on the ground, the average refractivity between 0 and 1 km can be estimated with an accuracy of around 3 mm/km. Using measurements at several sites at different heights, it is likely that this can be improved.

To test the inclusion of ground level refractivity data, we used simulations where we assumed that measurements of the refractivity of the voxels in the lowest layer were available with an accuracy of 1 mm/km. We used the eight- and 25-station networks and the profile simulated in Fig. 4. The assumed ground data were included as additional observations in the Kalman filter. The results indicated no significant improvement when including ground data. For the eight-station network, the average estimation error decreased to 1.74 mm/km, while for the 25-station network it increased slightly to 1.29 mm/km. The reason for the results not being much better when including ground measurements is that the geometry of the lowest layer is sufficiently good anyway (the stations are at different heights),
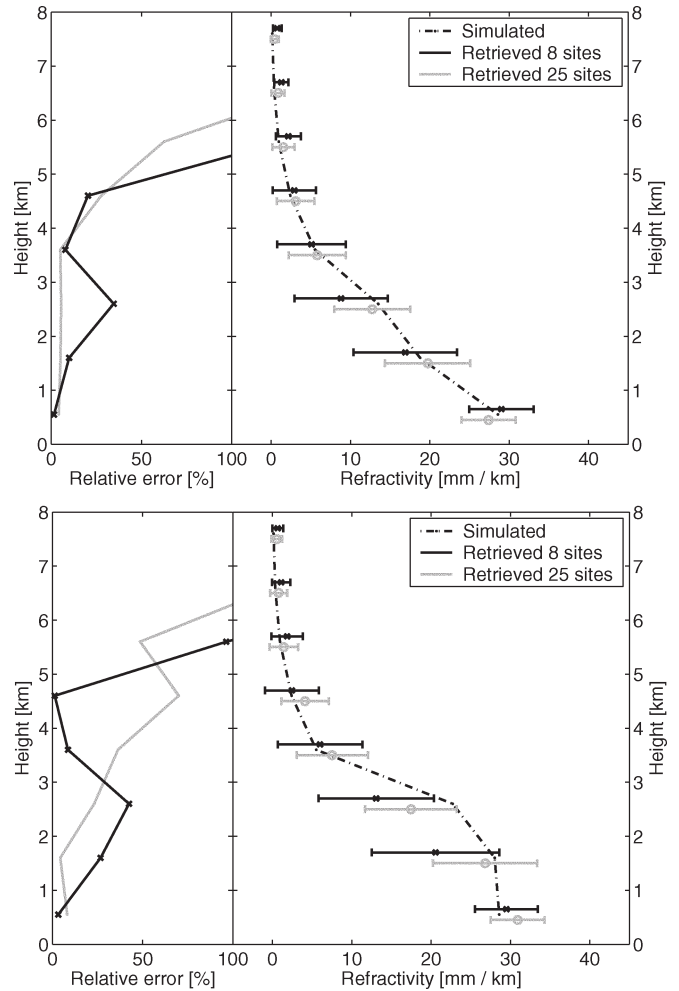

Fig. 12. Simulated and estimated wet refractivity profiles in real time using eight and 25 stations at (top) 9:00 and (bottom) 13:00. The rms observation noise was 10 mm.

and adding new information there will not have a significant impact on the retrieval quality. This will especially be true in the case of the 25-station network.

I. Real-Time Performance

When applying the method in real time, the situation will not be much different compared to the postprocessing of data. The largest additional difficulty in real time would be that the satellite orbits may be less accurate. Another issue of importance might be that the backward smoothing loop that we run on our results after the forward Kalman filter loop will not be used.

We made simulations where the satellite orbits had an accuracy of 5 m, which is of the same order of accuracy as the orbits broadcasted by the satellites. Since there are more accurate orbits available in real time, this can be considered a worst case scenario. In these simulations, we did not use the backward smoothing loop. We used both the eight- and 25-station networks and the profile in Fig. 4. The results were slightly worse than before, as seen in Fig. 12. The average estimation errors increased to 1.90 and 1.43 mm/km for the eight- and 25-station networks, respectively.

However, predicted orbits with much better accuracy than 5 m are normally available (e.g., the ultrarapid orbits from IGS [15]). If so, the estimated profiles will be better, almost as good as the postprocessing case. In near real time (i.e., a few hours delay), even better orbits can be available (probably as good as 20 cm or better, which is comparable to the orbits used in the postprocessing simulations in this paper). In this case, we would also be able to obtain an improved solution by using the backward loop. Hence, all the results presented in this paper could be regarded valid for a near-real-time application.

J. Comparison With Previously Used Method

Simulations comparing the new method presented in this paper to a previously developed one were also performed. In the previous methods, the slant wet delays were obtained by processing them using, for example, a Kalman filter (using the precise point positioning technique (PPP) [25]), in which the slant wet delays were modeled as functions of zenith wet delays and gradients together with the other unknown parts of the GPS signals (clock errors and integer ambiguities). After the initial GPS data processing (PPP), the retrieved slant wet delays (as given by the zenith delays and gradients) were used in WeRKaF [10], [11] to obtain the refractivity field.

The top plot in Fig. 13 shows the retrieval of the same profile as in the top plot of Fig. 3 using the eight-station network, and the bottom plot in Fig. 13 shows the retrieval of the same profile as in the bottom plot in Fig. 3 using the 25-station network. For simplicity, both profiles were without any gradients. The rms observation noise was 5 mm. Shown in the figures are the results using the new method: using WeRKaF with slant wet delays obtained from the GPS data processing, and using WeRKaF with slant wet delays being the true slant wet delays plus the observation noise. The latter case corresponds to an ideal case where all other contributions to the GPS phase observations are correctly estimated; hence, the remaining parts would be the slant wet delays plus the observation noise. This will however probably be impossible in reality.

As expected, the solution using "ideal" slant wet delays is performing best, followed by the new method. However, the solution using the slant wet delays obtained from the PPP solution is not performing very well, and the error is increasing with time. For the case of the top plot in Fig. 13, the mean estimation errors are 0.65, 5.54, and 1.78 mm/km for "ideal" slant wet delays, slant wet delays from the GPS PPP processing, and the new method, respectively. For the bottom plot in Fig. 13, these mean estimation errors are 1.65, 5.80, and 2.67 mm/km.

Looking at the lower plot in Fig. 13, we can see that the solution using the slant wet delays estimated using PPP actually detects a profile having a strong inversion, however with the maximum occurring at around 2.5 km instead of 1.5 km as in the simulated profile. This solution does not change significantly with time. Hence, this indicates that some of the information about the height distribution of the wet refractivity contained in the GPS phase observations has been lost in the PPP processing.

One way that might improve the estimation when using estimated slant wet delays is to add the residuals, although it
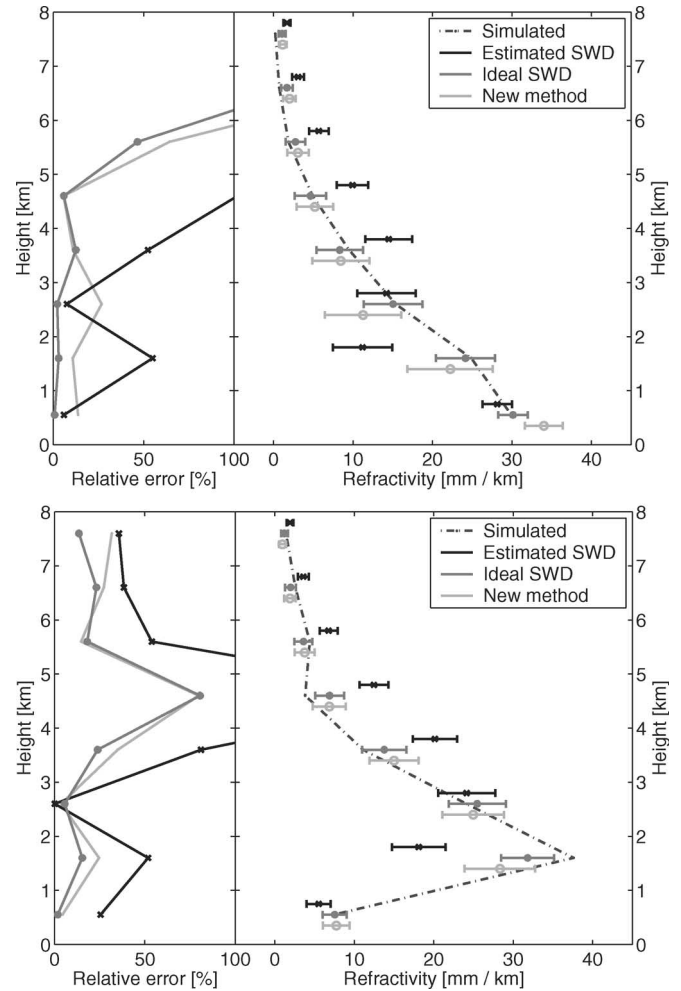

Fig. 13. Simulated and estimated refractivity profile using slant wet delays obtained using PPP (estimated SWD), "ideal" slant wet delays, and the new method. The upper plot uses the eight-station network, and the lower plot the 25-station network. The rms observation noise was 5 mm.

should be noted that such a procedure is not mathematically correct due to the inherent features of the method of least squares [12]. In some cases, adding the residuals can improve the accuracy of the retrieved slant wet delays while in other cases it will not, depending on how well it is possible to model the unmodeled wet atmosphere using the PPP model parameters. In our two simulations, we observed improvements when adding the residuals, but the profiles were still retrieved with errors with the same shape as before. The mean estimation errors were 3.55 and 4.24 mm/km for the top and bottom plots in Fig. 13, respectively.

In PPP processing, the only quantity not modeled correctly was the wet mapping function. Since the ratio between two slant wet delays at different elevation angles will depend on the shape of the wet refractivity profile, we need to know the wet refractivity profile to know the true mapping function. In our simulations, however, we consider the case when we have no knowledge of the wet refractivity profile; hence, we cannot know the true mapping function. Instead, we use the Niell [16] wet mapping function, which is based on an average profile for the latitude and does not consider the current state of the atmosphere. Hence, some of the information about the wet

refractivity profile contained in the slant wet delays will be lost in the PPP processing. Although this may be a small error, it is important because it is the wet refractivity profile we want to retrieve; hence, any loss of information on the water vapor distribution is unwanted. This is especially true in cases when low elevation angles are used, e.g., when we use a minimum elevation angle of $5°$.

V. Conclusion

We have presented a new tomographic method for retrieving the 3-D structure of the wet part of the tropospheric refractivity. This method has the advantage that it estimates the refractivity field directly from the raw GPS phase data.

As seen, the simulated refractivity fields were retrieved accurately when using a 25-station network. However, the simulations indicate that it will be difficult to retrieve the refractivity field with great accuracy when strong inversions are present using the existing Göteborg GPS network consisting of eight sites. This is because the network contains too few sites and is rather flat. The eight-station network can retrieve more complicated refractivity fields, e.g., containing strong inversions, but it requires a long time (> 12 h) to converge. In reality, such complicated refractivity fields may not be constant for such a long period. Initializing the Kalman filter with a good initial guess for the refractivity field would be one way to find the correct solution faster. However, simulations have shown that it is most important to initialize the Kalman filter with a refractivity field having a shape close to the correct one while being off by a constant scale factor will not make a large impact.

A network containing more sites (like the 25-station network we used in the simulations) or a network having a larger spread in station heights (as the nonflat network used in Section IV-F) will perform better. The simulations also show that using more than one GNSS will improve the retrievals.

The refractivities in the lowest layers are retrieved accurately in all simulations (except network 1 in Fig. 10). This is because of the better geometry in the lowest layer, the stations being located here and are at different heights (except in network 1 in Fig. 10). At higher levels, the geometry is much weaker due to the linear dependence of the observations, making the refractivity more difficult to retrieve.

As seen by the relative errors in the simulations, the method will not retrieve the refractivity accurately (in a relative sense) in the upper troposphere where the refractivity is very low. This is expected since the method is sensitive to the absolute refractivity (through slant wet delays). Also, the constraints in the Kalman filter are not allowing for much variation of the refractivity in the upper troposphere; hence, the refractivity there will be strongly dependent on the initial guess. To retrieve the refractivity in the upper troposphere, other methods should be used, such as, for example, the GPS occultation techniques [26].

In Appendix III, a few other possible model-based methods for retrieving the wet refractivity profile are presented. The best performing model is as good as the tomographic solution using 25 stations for the profile of the top plot in Fig. 3. The refractivity in this profile is almost exponentially decreasing

with height, which is the behavior of the wet refractivity of the atmosphere on average. Hence, it is not surprising that the model estimates it well. For the profile at the bottom plot in Fig. 3 and the changing profile in Fig. 4, the tomographic solution using 25 sites is better than the model. The refractivity of these profiles does not decrease exponentially with height in the middle of the day; hence, the model cannot be expected to perform as well in this case. This indicates that the GPS tomography will improve the estimation of refractivity when the wet refractivity distribution differs from the average.

When applying the method on real data, the results may be different from the ones presented here. It is difficult to model parts of the receiver noise such as multipath; hence, its effect might be different than from what was seen in the simulations. Furthermore, the variations in the refractivity simulated may not completely correspond to typical real variations in refractivity.

The next step in evaluating this method is to use real GPS data. A few preliminary results were presented in [27]. Other future developments of the method will include improvement of the model for the covariance matrix in the Kalman filter.

Appendix I
Estimation of the Hydrostatic Delay

The hydrostatic part of the refractivity can be written as [28]

$$N_h = k_1 R_d \rho \tag{16}$$

where k_1 is a constant, R_d is the specific gas constant of dry air, and ρ is the mass density of air. If hydrostatic equilibrium is assumed, we have

$$\frac{dP}{dz} = -\rho(z)g(z) \tag{17}$$

where $g(z)$ is the acceleration due to gravity at height z, and P the total pressure. By defining a mean acceleration due to gravity

$$g_m = \frac{\int_0^\infty \rho(z)g(z)dz}{\int_0^\infty \rho(z)dz} \tag{18}$$

the zenith hydrostatic delay can be calculated by using (16) and (17) as

$$l_h^z = 10^{-6} \int_o^\infty N_h \, dz = 10^{-6} k_1 R_d g_m^{-1} P_0 \tag{19}$$

where P_0 is the total pressure at the ground. By using an appropriate mapping function, the hydrostatic delay in any direction can be obtained.

In estimating the hydrostatic delay, we can identify three main possible error sources, namely: 1) uncertainties in the values of the constants used in the model (may give an error of $\sim 0.02\%$ [28]); 2) errors in the ground pressure measurements; and 3) errors introduced by the hydrostatic equilibrium assumption. To estimate how important the latter source is, an investigation was made using radiosonde data from Landvetter
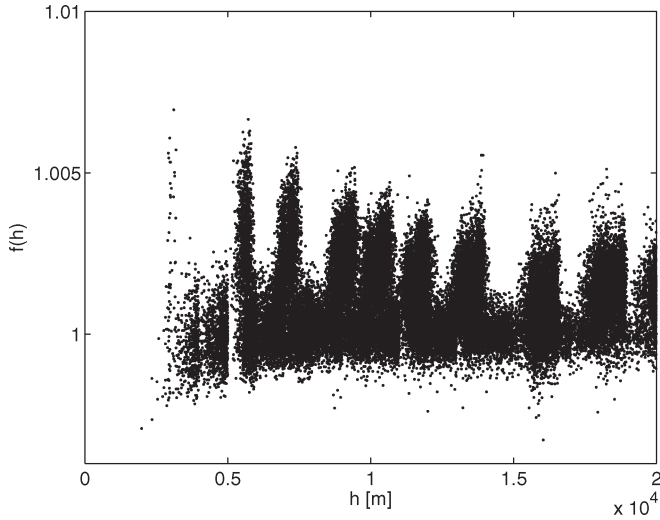
Fig. 14. $f(h)$ [see (22)] plotted as function of height h.

airport outside Göteborg. Using the ideal gas law, (17) can be rewritten as

$$\frac{1}{P}\frac{dP}{dz} = -\frac{g(z)}{R_d T(z)} \tag{20}$$

where $T(z)$ is the temperature. If we integrate the equation between $z = 0$ and $z = h$, we obtain

$$\ln\frac{P_0}{P_h} = \int\limits_0^h \frac{g(z)}{R_d T(z)} dz. \tag{21}$$

The ratio $g(z)/T(z)$ does not vary too much and too rapidly as a function of height, so if the integration on the right-hand side of (21) is done numerically, the error we introduce will be very small. Furthermore, if $h \ll R_E$, with R_E being the radius of the Earth, $g(z)$ will be approximately constant.

Using radiosonde data, both the left- and the right-hand sides of (21) could be calculated. Then, according to (21), the quantity

$$f(h) = \frac{\int_0^h \frac{g}{R_d T(z)} dz}{\ln\frac{P_0}{P_h}} \tag{22}$$

should be equal to 1. In Fig. 14, $f(h)$ is plotted as function of h based on radiosonde data from the period 1996–2002. As seen, $f(h)$ is close to 1. The deviations from 1 is of the same order as can be expected due to errors in the pressure and temperature measurements, typically 0.5 mbar and 0.2 °C, respectively [29].

Data from three radiosonde launches (all in the year 2000) were not included in Fig. 14. For these data, $f(h)$ deviated from unity of up to 2.5%. It is likely that these profiles contain errors due to faulty temperature measurements. The values recorded by the radiosondes were about 360 K at heights of 200–300 m.

Based on this investigation, an upper limit on the error in the hydrostatic delay introduced by the assumption of hydrostatic equilibrium is ~0.1%. However, since the deviation of $f(h)$ from 1 can be explained by errors in the radiosonde measurements, a definite limit on the validity of the assumption of

hydrostatic equilibrium could not be obtained. It is likely that the error could be much smaller than the above limit.

APPENDIX II
KALMAN FILTER

The chosen implementation of the Kalman filter is the alternative Kalman filter loop described in [19]. For more detailed information on the design of the refractivity part of the covariance matrix, see [11].

Let $N_w(h_1)$ and $N_w(h_2, R)$ denote the wet refractivity at two points at heights h_1 and h_2 and separated with the horizontal distance R. Then we can define a structure function for N_w as

$$D_{N_w}(h_1, h_2, R) = \left\langle [N_w(h_1) - N_w(h_2)]^2 \right\rangle \tag{23}$$

where the brackets denote the expectation value. By making the definitions

$$m_{N_w}(h) = \langle N_w(h) \rangle$$
$$\sigma_{N_w}^2(h) = \left\langle (N_w(h) - m_{N_w}(h))^2 \right\rangle \tag{24}$$
$$\mathrm{cov}\left[N_w(h_1), N_w(h_2, R)\right] = \langle N_w(h_1)N_w(h_2, R) \rangle$$
$$- m_{N_w}(h_1)m_{N_w}(h_2) \tag{25}$$

we can rewrite (23) as

$$D_{N_w}(h_1, h_2, R) = (m_{N_w}(h_1) - m_{N_w}(h_2))^2 + \sigma_{N_w}^2(h_2)$$
$$+ \sigma_{N_w}^2(h_2) - 2\mathrm{cov}\left[N_w(h_1), N_w(h_2, R)\right]. \tag{26}$$

According to [30], when $h_1 = h_2 = h$, this reduces to

$$D_{N_w}(h, h, R) = 2\sigma_{N_w}^2(h) - 2\,\mathrm{cov}\left[N_w(h), N_w(h, R)\right]$$
$$= \frac{R^{2/3}}{1 + \left(\frac{R}{L}\right)^{2/3}} C_N^2(h)$$
$$= C_R(R)C_N^2(h) \tag{27}$$

where L is the turbulence saturation scale length. Based upon this result, we formulate a model for $D_{N_w}(h_1, h_2, R)$ as

$$D_{N_w}(h_1, h_2, R) = (m_{N_w}(h_1) - m_{N_w}(h_2))^2$$
$$+ C_R(h_1, h_2, R)C_N^2(h_1, h_2). \tag{28}$$

Vertical variations may not be equivalent to horizontal variations. To take this into account, we introduce an adjustable constant C_0 and model C_R as

$$C_R = \frac{\left[R^2 + (h_1 - h_2)^2 C_0\right]^{1/3}}{1 + \left[\frac{R^2 + (h_1-h_2)^2 C_0}{L^2}\right]^{1/3}}. \tag{29}$$

A high value of C_0 means a low correlation between the refractivities at different heights; hence, the filter will rely more on the data than on the model for the height dependence of refractivity. On the other hand, the system may be weak in the vertical direction; hence, a high C_0 will also mean high sensitivity to noise. In the simulations, it was also found that $C_0 = 10^6$ was a good value for C_0.

Variations in time are assumed to be the result of a constant wind velocity V_w, so these variations can be described by the above model with $R = V_w t$, with t being the time. Assuming a wind speed of 8 m/s, $C_N^2(h_1, h_2)$ may be obtained from radiosonde data. Assuming that $C_N^2(h_1, h_2) = C_N(h_1) \cdot C_N(h_2)$, a simple model for C_N^2 was obtained from radiosonde launches separated by 6 and 12 h at the Landvetter airport outside Göteborg, i.e.,

$$C_N(h) = c_0 \exp\left[\left(\frac{h}{4460}\right)^3 - \left(\frac{h}{2270}\right)^2 + \frac{h}{1910}\right] \quad (30)$$

where $c_0 = 0.12$ mm/km m$^{-1/3}$. It was, however, found that a slightly lower c_0 ($c_0 = 0.04$ mm/km m$^{-1/3}$) gave better results in the simulations, so this value was used instead. Also, it was discovered that the results became much better when all distances in space were divided by a factor of 1000 when calculating the covariance matrix (while not changing distances in time). The reason for this may be that the correlations between the average refractivities of two voxels are somewhat different than the correlations between the refractivities of the midpoints of these voxels. A simple investigation revealed that the decreased correlation due to averaging may explain the factor 1000 in the correlation between neighboring voxels. Another reason for this factor may be that the effective voxel sizes are smaller in the lowest layers since there will be no GPS signals crossing the outer part of the outer voxels; hence, the method will not be sensitive to the refractivity there.

Using the above-derived $D_{N_w}(h_1, h_2, R)$, we can define the error covariance matrix needed in the Kalman filter implementation. The refractivities of the voxels are assumed to follow a random walk behavior. For consecutive samples k and $k+1$ of voxels i and j, we have

$$(N_w)_i(k+1) = (N_w)_i(k) + w_i$$
$$(N_w)_j(k+1) = (N_w)_j(k) + w_j \quad (31)$$

where w is the driving noise. We assume the variance of this driving noise to be constant in time. The covariance between samples i and j for sampling interval T then becomes

$$Q_{ij} = \langle((N_w)_i(k+1) - (N_w)_i(k)) \cdot ((N_w)_j(k+1) - (N_w)_j(k))\rangle$$
$$= D_{N_w}(h_1, h_2, R, T) - D_{N_w}(h_1, h_2, R)$$
$$= \left[\frac{r_f^{2/3}}{1 + (r_f/L)^{2/3}} - \frac{R_f^{2/3}}{1 + (R_f/L)^{2/3}}\right] \quad (32)$$

where

$$R_f^2 = R^2 + (h_1 - h_2)^2 C_0$$
$$r_f^2 = R_f^2 + (V_w \cdot T)^2. \quad (33)$$

For the clock errors, white noise processes were assumed. This assumption is not necessarily true: there might be correlations between the clock error at two different time epochs. However, assuming white noise in this case will not be wrong since by doing that we only assume the worst case scenario

(i.e., that knowledge of the clock error at a previous time epoch will not help in estimating the clock error at the present epoch). Hence, for two clock errors i and j for consecutive samples k and $k+1$, we have

$$\tau_i(k+1) = u_i \quad \tau_j(k+1) = u_j \quad (34)$$

where u is a white noise process. Their variances σ_u^2 are assumed to be equal and independent in time and of each other. An investigation of real GPS data indicated that the standard deviations of the clock errors (including the orbit errors and common parts of the integer ambiguities) σ_u were about 10^5 m ($\sim$1 ms). The clock part of the covariance matrix then becomes

$$Q_{ij} = \langle(\tau_i(k+1) - \tau_i(k))(\tau_j(k+1) - \tau_j(k))\rangle$$
$$= \langle u_i u_j\rangle = \begin{cases} \sigma_u^2, & i = j \\ 0, & i \neq j. \end{cases} \quad (35)$$

The Kalman filter is initialized by an initial guess for the refractivities (no special initial guess for the clock errors is needed because we assume that they are zero-mean white-noise processes). The initial guess for the wet refractivity profile used in our simulations was an exponential profile with a scale height of 2 km and with ground value of 40 mm/km, which is approximately what we will obtain if we take an average profile of all profiles obtained from radiosondes during one year. After the full Kalman filter loop, a standard backward loop [19] is run to get smoother and hence possibly more accurate results.

APPENDIX III
REFRACTIVITY ESTIMATION USING SIMPLE METHODS

The refractivity profile can be retrieved using other simpler methods than the GPS tomography. We have considered four methods, namely: 1) using pure statistics (i.e., estimating the refractivity based on the day of the year); 2) using ground data (i.e., having measurement of the refractivity at the ground); 3) using a single GPS receiver (or another instrument which can measure the zenith wet delay, e.g., a water vapor radiometer); and 4) having both ground data and one GPS receiver.

We divided the atmosphere into eight layers, each with a height of 1 km, and calculated the average refractivity in each layer from each radiosonde launch along with the integrated refractivity (zenith wet delay) and the refractivity on the ground. The models for the wet refractivity used are described by

$$N(k) = a_1(k) + a_2(k)\sin\left(2\pi\frac{D}{365} + a_3(k)\right) \quad (36)$$

$$N(k) = b_1(k) + b_2(k)N_0 \quad (37)$$

$$N(k) = c_1(k) + c_2(k)l_z \quad (38)$$

$$N(k) = d_1(k) + d_2(k)N_0 + d_3(k)l_z \quad (39)$$

where $N(k)$ is the refractivity in layer k, N_0 is the refractivity at the ground, l_z the zenith wet delay, D is the day of the year, and $a_i(k)$, $b_i(k)$, $c_i(k)$, and $d_i(k)$ are constants. The constants were obtained from a least square fit to three years of radiosonde

TABLE I
VALUES FOR THE CONSTANTS OF MODELS (36) AND (37). REFRACTIVITY
IS MEASURED IN MILLIMETERS PER KILOMETER AND a_3 IS IN DEGREES

k	$a_1(k)$	$a_2(k)$	$a_3(k)$	$b_1(k)$	$b_2(k)$
1	37.242	-14.903	56.3	-0.052	0.833
2	23.841	-10.398	62.0	-2.170	0.583
3	14.636	-6.738	63.2	-2.637	0.388
4	9.124	-4.116	60.5	-1.534	0.239
5	5.661	-2.590	58.2	-0.987	0.149
6	3.182	-1.476	57.1	-0.423	0.081
7	1.730	-0.880	56.0	-0.321	0.046
8	0.871	-0.509	56.4	-0.268	0.025

TABLE II
VALUES FOR THE CONSTANTS OF MODELS (38) AND (39). REFRACTIVITY
IS MEASURED IN MILLIMETERS PER KILOMETER AND
WET DELAY IS MEASURED IN MILLIMETERS

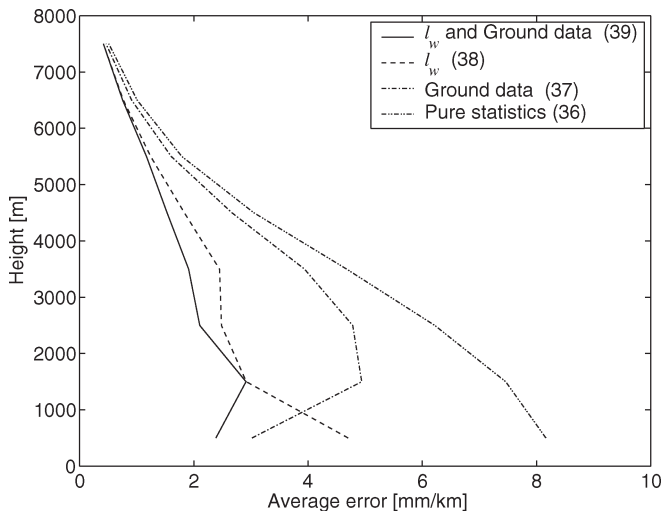| k	$c_1(k)$	$c_2(k)$	$d_1(k)$	$d_2(k)$	$d_3(k)$
1	9.540	0.287	0.766	0.097	0.604
2	0.518	0.243	-0.277	0.226	0.055
3	-3.319	0.187	-0.570	0.246	-0.189
4	-3.019	0.126	0.088	0.193	-0.214
5	-1.965	0.079	0.040	0.122	-0.138
6	-0.926	0.043	0.125	0.065	-0.072
7	-0.522	0.023	-0.038	0.034	-0.033
8	-0.306	0.012	-0.135	0.016	-0.012

Fig. 15. Average error of the refractivity estimations using the different methods described in the text.

data. The obtained values of the constants are shown in Tables I and II.

Fig. 15 shows how well the four models agree with real data. Plotted are the average deviation between the models and the radiosonde data. The data used are four years of radiosonde data, which were data not used in the coefficient estimate of the models. On average, the deviations were 4.1, 2.8, 2.1, and 1.6 mm/km for the methods when using pure statistics, ground data, zenith wet delay, and both ground data and zenith wet delay, respectively.

The best of the methods (39) estimates the exponential profile in Fig. 3 with an average estimation error of 1.1 mm/km, i.e., about the same accuracy as the tomographic estimation when using the 25-station network. The profile with an inversion in Fig. 3 is, however, only estimated with an average estimation error of 5.01 mm/km, better than the eight-station network but

clearly worse than the 25-station network. The mean estimation error when estimating the profile in Fig. 4 is 1.59 mm/km, which is better than the tomographic solution from the eight-station network but worse than the solution from the 25-station network. The change in the refractivity that occurs in this profile has its maximum in the middle of the grid, i.e., the change is not so strong in the outer voxels. The model (39) estimation of the profile is worst in the middle (mean estimation error 1.87 mm/km), while the tomographic estimations are best in the middle of the grid where the stations are located (mean estimation error of 1.79 and 1.26 mm/km using eight and 25 stations, respectively). This confirms the usefulness of the tomographic method in situations when nonstandard profiles (containing inversions, etc.) are present.

REFERENCES

[1] C. Rocken, T. V. Hove, J. Johnson, F. Solheim, R. Ware, M. Bevis, S. Chiswell, and S. Businger, "GPS/STORM-GPS sensing of atmospheric water vapor for meteorology," *J. Atmos. Ocean. Technol.*, vol. 12, no. 3, pp. 468–478, Jun. 1995.
[2] P. Tregoning, R. Boers, D. O'Brien, and M. Hendy, "Accuracy of absolute precipitable water vapor estimates from GPS observations," *J. Geophys. Res.*, vol. 103, no. D22, pp. 28 701–28 710, Nov. 1998.
[3] T. R. Emardson, G. Elgered, and J. M. Johansson, "Three months of continuous monitoring of atmospheric water vapor with a network of global positioning system receivers," *J. Geophys. Res.*, vol. 103, no. D2, pp. 1807–1820, 1998.
[4] G. Ruffini, A. Flores, and A. Rius, "GPS tomography of the ionospheric electron content with a correlation functional," *IEEE Trans. Geosci. Remote Sens.*, vol. 36, no. 1, pp. 143–153, Jan. 1998.
[5] A. Flores, J. V.-G. de Arellano, L. P. Gradinarsky, and A. Ruis, "Tomography of the lower troposphere using a small dense network of GPS receivers," *IEEE Trans. Geosci. Remote Sens.*, vol. 39, no. 2, pp. 439–447, Feb. 2001.
[6] M. Troller, B. Bürki, M. Cocard, A. Geiger, and H.-G. Kahle, "3-D refractivity field from GPS double difference tomography," *Geophys. Res. Lett.*, vol. 29, no. 24, p. 2149, Dec. 2002.
[7] H. Seko, S. Shimada, H. Nakamura, and T. Kato, "Three-dimensional distribution of water vapor estimated from tropospheric delay of GPS data in a mesoscale precipitation system of the Baiu front," *Earth Planets Space*, vol. 52, no. 11, pp. 927–933, Nov. 2000.
[8] A. E. MacDonald, Y. Xie, and R. H. Ware, "Diagnosis of three-dimensional water vapor using a GPS network," *Mon. Weather Rev.*, vol. 130, no. 2, pp. 386–397, Feb. 2002.
[9] C. Champollion, F. Mason, M.-N. Bouin, A. Walpersdorf, E. Doerflinger, O. Bock, and J. van Baelen, "GPS water vapour tomography: Preliminary results from the ESCOMPTE field experiment," *Atmos. Res.*, vol. 74, no. 1–4, pp. 253–274, Mar. 2005.
[10] L. Gradinarsky and P. Jarlemark, "Ground-based GPS tomography of water vapor: Analysis of simulated and real data," *J. Meteorol. Soc. Jpn.*, vol. 82, no. 1, pp. 551–560, Feb. 2004.
[11] L. P. Gradinarsky. (2002). "Sensing atmospheric water vapor using radio waves," Ph.D. dissertation, Chalmers Univ. Technol., Göteborg, Sweden. Tech. Rep. 436. [Online]. Available: http://www.oso.chalmers.se/dwl/lubo/Thesis.pdf
[12] P. Elósegui and J. Davis, "Accuracy assessment of GPS slant-path determinations," in *Proc. Int. Workshop GPS Meteorol.*, Tsukuba, Japan, 2003, p. 1-35-1. [Online]. Available: http://dbx.cr.chiba-u.jp/Gps_Met/gpsmet/index.html

[13] T. Nilsson, L. P. Gradinarsky, and G. Elgered, "GPS tomography using phase observations," in *Proc. IGARSS*, 2004, vol. 4, pp. 2756–2759.

[14] B. Hofmann-Wellenhof, H. Lichtenegger, and J. Collins, *GPS: Theory and Practice*, 5th ed. New York: Springer-Verlag, 2001.

[15] G. Beutler, M. Rothacher, S. Schaer, T. A. Springer, J. Kouba, and R. E. Neilan, "The International GPS Service (IGS): An interdisciplinary service in support of Earth sciences," *Adv. Space Res.*, vol. 23, no. 4, pp. 631–635, 1999.

[16] A. E. Niell, "Global mapping function for the atmospheric delay at radio wavelengths," *J. Geophys. Res.*, vol. 101, no. B2, pp. 3227–3246, Feb. 1996.

[17] F. K. Brunner and M. Gu, "An improved model for dual frequency ionospheric correction of GPS observations," *Manuscr. Geod.*, vol. 16, no. 3, pp. 205–214, 1991.

[18] Z. Wang, Y. Wu, and K. Zhang, "Triple-frequency methods for high-order ionospheric refractive error modelling in GPS modernization," in *Proc. Int. Symp. GNSS/GPS*, 2004, pp. 291–295.

[19] R. G. Brown and P. Y. C. Hwang, *Introduction to Random Signals and Applied Kalman Filtering*, 3rd ed. Hoboken, NJ: Wiley, 1997.

[20] L. P. Gradinarsky and G. Elgered, "Horizontal gradients in the wet path delay derived from four years of microwave radiometer data," *Geophys. Res. Lett.*, vol. 27, no. 16, pp. 2521–2524, Aug. 2000.

[21] K. Borre and C. Tiberius, "Time series analysis of GPS observables," in *Proc. 13th Int. Tech. Meeting Satellite Division Inst. Navigat. GPS*, 2000, pp. 1885–1894.

[22] R. B. Langley, "GLONASS: Review and update," *GPS World*, vol. 8, no. 7, pp. 46–51, 1997.

[23] The Galilei Project—GALILEO Design Consolidation. (2003). European Commision. [Online]. Available: http://ec.europa.eu/dgs/energy_transport/galileo//documents/technical_en.htm

[24] P. Elósegui, J. L. Davis, L. P. Gradinarsky, G. Elgered, J. M. Johansson, D. A. Tahmoush, and A. Rius, "Sensing atmospheric structure using small-scale space geodetic networks," *Geophys. Res. Lett.*, vol. 26, no. 16, pp. 2445–2448, Aug. 1999.

[25] J. F. Zumberge, M. B. Heflin, D. C. Jefferson, M. M. Watkins, and F. H. Webb, "Precise point positioning for the efficient and robust analysis of GPS data from large networks," *J. Geophys. Res.*, vol. 102, no. B3, pp. 5005–5017, Mar. 1997.

[26] U. Foelsche and G. Kirchengast, "Tropospheric water vapor imaging by combination of ground-based and spaceborne GNSS sounding data," *J. Geophys. Res.*, vol. 106, no. D21, pp. 27 221–27 231, 2001.

[27] T. Nilsson, L. Gradinarsky, and G. Elgered, "Estimating the 3D structure of the atmospheric water vapor using GPS phase observations," in *Proc. RVK*, Linköping, Sweden, 2005, pp. 521–526. [Online]. Available: http://www.es.isy.liu.se/rvk05/_final/00085Uy1iigccqA_PxHNvocCC.pdf

[28] J. L. Davis, T. A. Herring, I. I. Shapiro, A. E. E. Rogers, and G. Elgered, "Geodesy by radio interferometry: Effects of atmospheric modeling errors on baseline length," *Radio Sci.*, vol. 20, no. 6, pp. 1593–1607, 1985.

[29] *"Vaisala Radiosonde HRS29-SGP Brochure*," Ref. B210358EN-C, Vaisala Oyj, Helsinki, Finland, 2006. [Online]. Available: http://www.vaisala.com/businessareas/measurementsystems/soundings/products/radiosond

[30] R. N. Treuhaft and G. E. Lanyi, "The effect of the dynamic wet troposphere on radio interferometric measurements," *Radio Sci.*, vol. 22, no. 2, pp. 251–265, 1987.

Tobias Nilsson was born in Svenljunga, Sweden, on October 7, 1978. He received the M.Sc. degree in engineering physics from Uppsala University, Uppsala, Sweden, in 2003, and the Licentiate of Engineering degree from the Chalmers University of Engineering, Göteborg, Sweden, in 2005. He is currently working toward the Ph.D. degree at the Chalmers University of Technology.

Lubomir Gradinarsky was born in Sofia, Bulgaria, in 1970. He received the M.S.E.E and Ph.D. degrees from the Chalmers University of Technology, Göteborg, Sweden, in 1996 and 2002, respectively.

He is currently a Senior Scientist at Sensor Technology, Astra-Zeneca R&D, Mölndal, Sweden. His research has been focused on the remote sensing of the atmosphere using space geodetic techniques and microwave radiometry. His work also includes the development of remote sensing techniques for industrial applications.